Nano Research 2014, 7(12): 1861–1872
DOI 10.1007/s12274-014-0546-4
Research Article

ISSN 1998-0124
CN 11-5974/O4

Dyeing bacterial cellulose pellicles for energetic heteroatom doped carbon nanofiber aerogels

Zhen-Yu Wu[§], Hai-Wei Liang[§], Chao Li, Bi-Cheng Hu, Xing-Xing Xu, Qing Wang, Jia-Fu Chen, and Shu-Hong Yu (✉)

Division of Nanomaterials and Chemistry, Hefei National Laboratory for Physical Sciences at Microscale, Collaborative Innovation Center of Suzhou Nano Science and Technology, Department of Chemistry, University of Science and Technology of China, Hefei, Anhui 230026, China

[§] These authors contributed equally to this work.

Received: 8 June 2014
Revised: 14 July 2014
Accepted: 18 July 2014

KEYWORDS

doped carbon nanofiber aerogels,
electrocatalysts,
oxygen reduction reaction,
supercapacitors,
organic dyes,
bacterial cellulose

ABSTRACT

The energy crisis and environmental pollution are serious challenges that humanity will face for the long-term. Despite tremendous efforts, the development of environmentally friendly methods to fabricate new energy materials is still challenging. Here we report, for the first time, a new strategy to fabricate various doped carbon nanofiber (CNF) aerogels by pyrolysis of bacterial cellulose (BC) pellicles which had adsorbed or were dyed with different toxic organic dyes. The proposed strategy makes it possible to remove the toxic dyes from waste–water and then synthesize doped CNF aerogels using the dyed BC pellicles as precursors. Compared with other reported processes for preparing heteroatom doped carbon (HDC) nanomaterials, the present synthetic method has some significant advantages, such as being green, general, low-cost and easily scalable. Moreover, the as-prepared doped CNF aerogels exhibit great potential as electrocatalysts for the oxygen reduction reaction (ORR) and as electrode materials for supercapacitors.

1 Introduction

The development of high performance, low cost, and environmentally friendly electrochemical energy conversion and storage systems, such as fuel cells, dye-sensitized solar cells, supercapacitors, lithium-ion and metal-air batteries, is an important step on the road to alternative energy technologies [1–7]. Due to their electronic characteristics, and surface and local features, heteroatom (N, B, S and P) doped carbon (HDC) nanomaterials show great potential applications in such devices [8–13]. For example, HDC nanomaterials have been considered as promising electrocatalysts for oxygen reduction reactions (ORR) in fuel cells and metal–air batteries to overcome some instinctive drawbacks of platinum- or palladium-

---

Address correspondence to shyu@ustc.edu.cn

based catalysts, such as high cost, limited supply, crossover deactivation and poor durability [14–19]. On the other hand, when used as supercapacitor electrode materials, HDC nanomaterials exhibit excellent capacitive performance (such as large electrochemical capacitance, good retention capability, high power density, and long-term cycling stability) due to the cooperative effects of electrical double-layer capacitance (EDLC) and pseudocapacitance [11, 20–22].

Recently, many methods have been developed to synthesize HDC nanomaterials. The existing approaches can be categorized into two main types: direct synthesis and post treatment [17, 23]. The direct synthesis route includes chemical vapor deposition (CVD) [24, 25], segregation growth approaches [26], and solvothermal [27] and arc-discharge methods [28]. Normally, these complex processes need special apparatus and rigorous conditions, hampering their widespread applications. In addition, the extremely low yield limits their applications only to fundamental studies. Post treatment methods, such as thermal treatment in a heteroatom-donor atmosphere or with heteroatom-rich compounds [29–31] and plasma treatment [32], have been widely used to prepare various doped carbon nanomaterials with different heteroatom species, controllable doping contents, and unique morphologies. However, most of the approaches inevitably involve expensive and toxic precursors, making them unsuitable for practical application. Therefore, it is highly desirable—but remains challenging—to develop a general, low-cost, eco-friendly, and easily scalable method to produce HDC nanomaterials.

Organic dyes are widely used for coloring in many industries, such as textiles, paper, printing, plastic, pharmaceuticals, leather, cosmetics, and food, and the effluents from these industries tend to contain dyes in excessive quantities [33, 34]. Certain dyes and their degradation counterparts are potentially carcinogenic and toxic, therefore, their presence in water poses serious threats to aquatic life and human populations [35, 36]. Thus, removal of these toxic and carcinogenic dyes from waste–water has recently attracted more attention to prevent further deterioration of water resources. Considering the rich amount of heteroatoms in various organic dyes, they can be used as precursors to prepare HDC nanomaterials. This inspired us to remove harmful dyes from the effluents with a carbonaceous material sorbent and then employ the sorbent saturated with dyes to fabricate HDC nanomaterials for electrochemical energy conversion and storage. The proposed strategy makes it possible to remove the toxic dyes from waste–water and synthesize HDC nanomaterials simultaneously. Most importantly, it makes harmful waste profitable.

Bacterial cellulose (BC), a typical biomass material, can be produced on an industrial scale via the microbial fermentation process [37, 38]. Our recent studies demonstrated that the low cost and environmentally friendly BC pellicles are excellent precursors for producing ultralight, flexible, and highly conductive carbon nanofiber (CNF) aerogels [39–41]. Here we report, for the first time, a novel method to fabricate various doped CNF aerogels by employing the BC pellicles which have adsorbed or been dyed with different toxic organic dyes as precursors. Compared with other reported processes for preparing HDC nanomaterials, our synthetic method has some significant advantages, namely, (1) the use of organic dyes in waste–water for preparing doped CNF aerogels, turns toxic waste into a valuable material; (2) it is low-cost, environmentally friendly, easy to scale up, and suitable for different carbonaceous precursors to prepare HDC nanomaterials; (3) the high heteroatom content and three-dimensional (3D) network structure of as-prepared doped CNF aerogels gives them great application potential.

2 Results and discussion

Doped CNF aerogels were prepared through a three-step process as illustrated in Fig. 1(a) (see the Experimental section for details of the synthesis). Small BC hydrogels were first soaked in various organic dye solutions for three days, making them adsorb dyes until saturation (Step 1). Then, the obtained BC/dye hybrid hydrogels were subjected to freeze-drying to remove water from the wet gels (Step 2). Finally, the variously colored dried BC/dye hybrid aerogels were pyrolyzed under a flowing N_2 atmosphere to generate black doped CNF aerogels

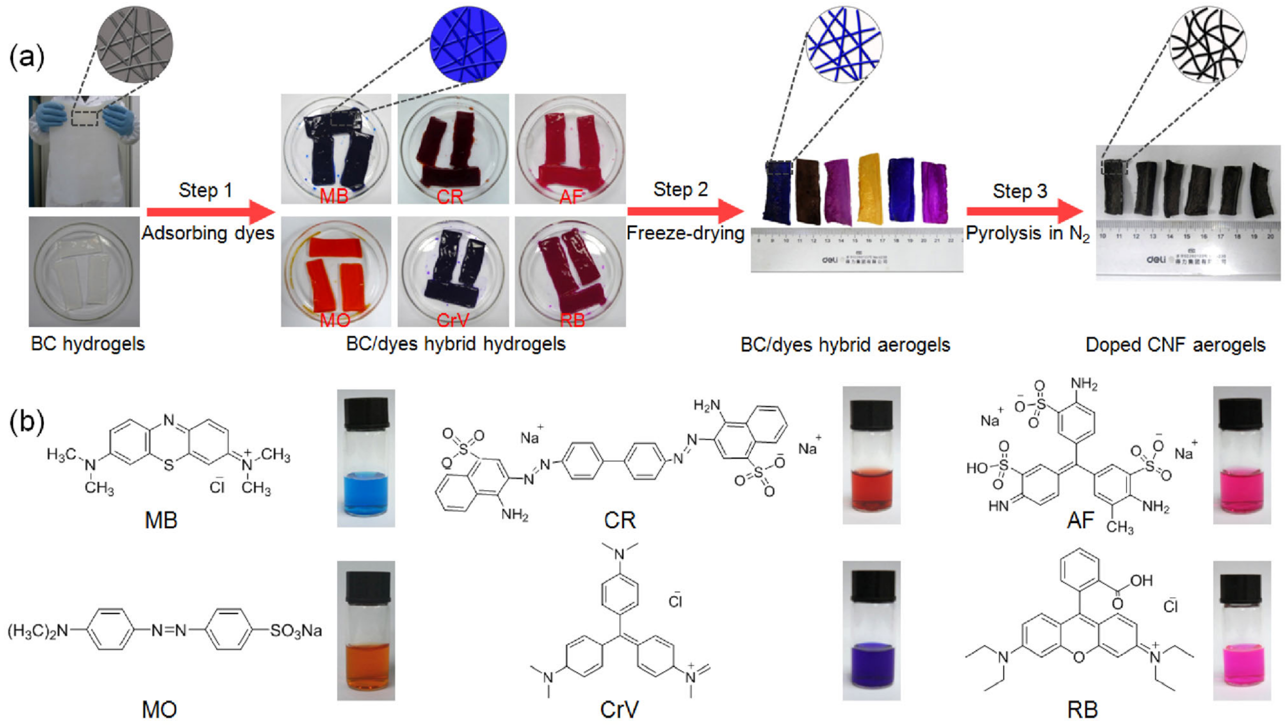

Figure 1 The fabrication process of doped CNF aerogels. (a) (1) BC hydrogels were soaked in various organic dye solutions (imitating waste–water) until saturation sorption; (2) after freeze-drying of the as-obtained BC/dye hybrid hydrogels, various BC/dye hybrid aerogels were obtained; (3) further pyrolysis of BC/dye hybrid aerogels under flowing N_2 produced doped CNF aerogels. (b) Molecular formulae of organic dyes (methylene blue, Congo red, acid fuchsin, methyl orange, crystal violet, and Rhodamine B) used in the fabrication process and corresponding digital images of their solutions. The high heteroatom contents in organic dyes make them be excellent precursors for preparing doped CNF aerogels.

(Step 3). The advantages of the present method are its green preparation process and universality in HDC nanomaterial fabrication. With abundant functional groups (such as –O–H, C=O, and C–O) and unique 3D architectures [37, 39], BC pellicles are excellent candidates as sorbents for various dyes in their aqueous solutions (imitating waste–water). In this study, methylene blue (MB), Congo red (CR), acid fuchsin (AF), methyl orange (MO), crystal violet (CrV), and Rhodamine B (RB) were chosen as typical model dyes to prepare doped CNF aerogels (Fig. 1(b)); BC pellicles exhibited high sorption capacities of 97.8, 205.4, 75.1, 107.2, 148.0, and 153.7 $mg\cdot g^{-1}$ for MB, CR, AF, MO, CrV and RB, respectively. As a result, a series of doped CNF aerogels were obtained by using these dyes, indicating the strategy described above is quite general. The as-prepared doped CNF aerogels are referred to as x-CNF-y (z), where x, y and z are the species of doped heteroatoms, pyrolysis temperature and the dyes adsorbed by BC in preparation process, respectively. For the purpose of comparison, the undoped CNF aerogels (denoted as CNF aerogels) were also prepared (see Fig. S1 in the Electronic Supplementary Material (ESM)). As far as we know, this is the first report of a process for turning harmful waste into a valuable material to prepare various HDC nanomaterials. In addition, other carbon-rich precursors (e.g., hydrothermal carbon materials, activated carbon, and other biomass) can also be converted into HDC materials through the present method, promising its widespread application.

The morphologies and chemical compositions of all as-prepared samples were investigated by various characterization techniques to prove the feasibility of the proposed method in fabricating doped CNF aerogels (Fig. 2, and Figs. S2–S6 and Table S1 in the ESM). We chose N-S-CNF-800 (MB) as a typical example to demonstrate them clearly. The microstructure of N-S-CNF-800 (MB) aerogel was first characterized by scanning electron microscopy (SEM)

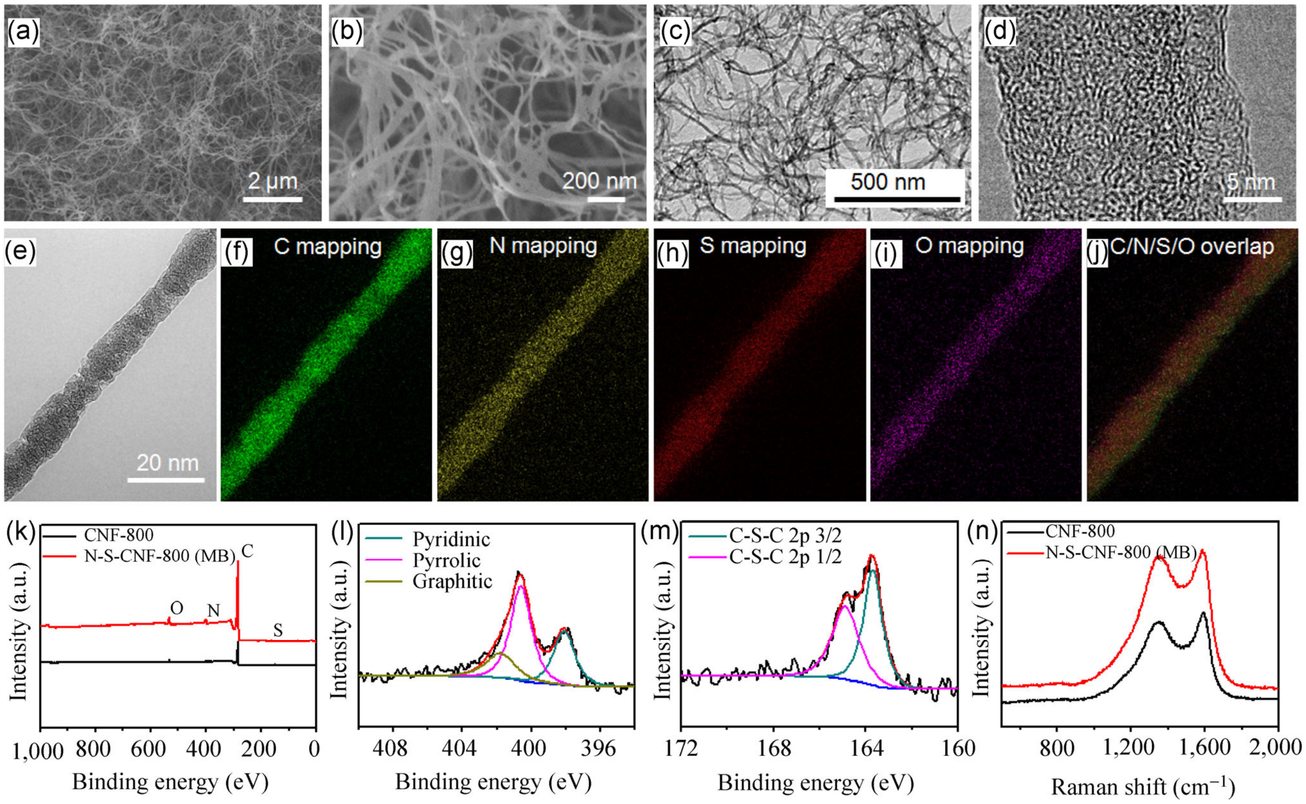

Figure 2 The morphologies and chemical compositions of N-S-CNF-800 (MB). (a) and (b) SEM images and (c) TEM image of N-S-CNF-800 (MB) aerogel revealing its 3D network nanostructure with 10–20 nm nanofibers. (d) HRTEM image of an individual N-S-CNF-800 (MB). (e)–(j) Energy filter TEM (EFTEM) image and elemental mapping of an individual N-S-CNF-800 (MB). (k) XPS survey spectra of N-S-CNF-800 (MB) and CNF-800. High-resolution XPS spectra of the deconvoluted (l) N 1s peak and (m) S 2p peak of N-S-CNF-800 (MB). (n) Raman spectra of N-S-CNF-800 (MB) and CNF-800.

and transmission electron microscopy (TEM). The resulting N-S-CNF-800 (MB) aerogel has a 3D network nanostructure with 10–20 nm nanofibers and many interconnected pores (Figs. 2(a)–2(c)). Remarkably, these nanofibers interconnect with each other by many junctions, resulting in excellent conductive and mechanical properties. The high resolution TEM image further reveals that these nanofibers are mainly made up of randomly orientated graphitic layers, although turbostratic carbon may exist in the nanofibers (Fig. 2(d)). The doping of heteroelements into CNF aerogel was first probed by EFTEM. The EFTEM mapping indicates the presence of C, N, S, and O elements in the nanofiber. The overlap mapping image clearly shows that N and S atoms are homogeneously distributed in N-S-CNF-800 (MB) (Figs. 2(e)–2(j)). Considering that the MB precursors can be completely decomposed at high temperatures, it is reasonable to believe the N and S atoms have been successfully introduced into carbon framework via covalent bonds, rather than any residual MB being present. The result is also evidenced by the following X-ray photoelectron spectroscopy (XPS) measurement of N-S-CNF-800 (MB), as no peak of Cl 2p (a typical peak of MB) is found.

The chemical status of these elements was further investigated by XPS. The XPS survey spectrum in Fig. 2(k) shows a dominant C 1s peak (~284.5 eV), an O 1s peak (~532.0 eV), a N 1s peak (~400.8 eV), and a S 2p peak (~164.8 eV), which further confirms the successful doping of N and S in as-prepared N-S-CNF-800 (MB). Comparison of the XPS results before and after pyrolysis in N_2 clearly indicates the N and S doping are caused by the pyrolysis process (Fig. S7 in the ESM). The N and S elemental contents of N-S-CNF-800 (MB) are 4.64 at.% and 0.91 at.%, respectively. The N 1s spectrum can be deconvoluted into three peaks: 398.6 eV ± 0.3 eV, 400.5 eV ± 0.3 eV, 401.3 eV ± 0.3 eV, corresponding to pyridinic N, pyrrolic N, and graphitic N, respectively (Fig. 2(l)) [42, 43]. The high-resolution S 2p spectrum can be fitted with two peaks at ~163.8 and ~165 eV, which are in agreement with the reported $2p_{3/2}$ and $2p_{1/2}$ positions of thiophene-S owing to their spin-orbit coupling; SO_x groups (~168.5 eV), which are chemically inactive, are not evident (Fig. 2(m)) [19, 44, 45]. Further electronic and structural information about N-S-CNF-800 (MB) was obtained from Raman spectroscopy. As illustrated in Fig. 2(n), the Raman spectra of N-S-CNF-800 (MB) and pristine CNF-800 aerogel exhibit two significant peaks at ~1,355 cm^{-1} and ~1,590 cm^{-1}, corresponding to the D band and G band, respectively. The D band is related to disordered structure or graphene edges, while the G band is assigned to the vibration of all sp^2 hybridized carbon atoms of the carbon layers. The intensity ratio I_D/I_G (the intensity of the D-band divided by the intensity of the G-band) is widely used to assess the density of defects in graphite materials [10, 13, 16]. The value of I_D/I_G increases from 0.92 for CNF-800 to 0.98 for N-S-CNF-800 (MB), indicating that there are more defect sites in sp^2-carbon hexagonal network of N-S-CNF-800 (MB) created by N and S doping. Meanwhile, the results shown in Figs. S2–S6 and Table S1 clearly prove successful fabrication of other doped CNF aerogels, indicating that the present strategy is a highly effective and general way to prepare HDC nanomaterials.

With their 3D network architecture, interconnected porosity, graphitic carbon structure and high heteroatom contents, the as-prepared doped CNF aerogels are ideal candidates as electrocatalysts for ORR. The electrocatalytic performance of N-S-CNF-800 (MB) was first investigated by cyclic voltammetry (CV) at a scan rate of 50 $mV\cdot s^{-1}$ in N_2- and O_2-saturated 0.1 M aqueous KOH electrolyte solutions (Fig. 3(a)). In the case of a N_2-saturated solution, the CV curve within the potential range –0.8 to +0.2 V presents the pseudocapacitive behavior of doped nanocarbon materials. In contrast, a well-defined cathodic peak centered at –0.39 V appears in the CV when the electrolyte

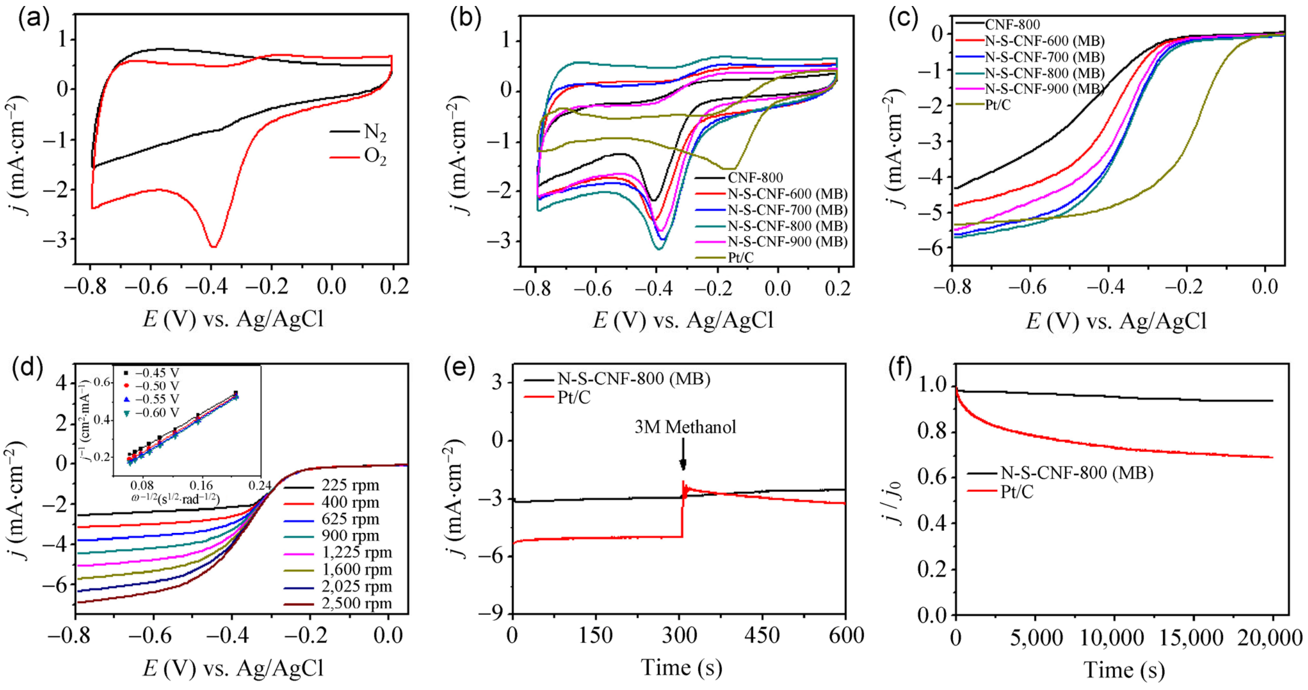

Figure 3 ORR performance of N-S-CNF-*y* (MB) aerogels and reference catalysts. (a) CV curves of N-S-CNF-800 (MB) in N_2- and O_2-saturated 0.1 M aqueous KOH electrolyte at a scan of 50 $mV\cdot s^{-1}$. (b) CV curves of CNF-800, N-S-CNF-600, 700, 800, 900 (MB), and Pt/C catalyst in O_2-saturated 0.1 M aqueous KOH electrolyte at a scan of 50 $mV\cdot s^{-1}$. (c) LSVs of the above samples at a scan of 10 $mV\cdot s^{-1}$, electrode rotating rate: 1,600 rpm. (d) LSVs of N-S-CNF-800 (MB) with various rotation rates at a scan of 10 $mV\cdot s^{-1}$. The inset in (d) shows the corresponding Koutecky–Levich plots (j^{-1} vs. $\omega^{-1/2}$) at different potentials. (e) Chronoamperometric responses to the addition of 3 M methanol of N-S-CNF-800 (MB) and Pt/C catalyst modified electrodes at –0.4 V and a rotation speed of 1,600 rpm. (f) Durability evaluation of N-S-CNF-800 (MB) and Pt/C catalyst for 20,000 s at –0.4 V and a rotation speed of 1,600 rpm.

solution is saturated with O_2, suggesting a pronounced electrocatalytic activity of the as-prepared N-S-CNF-800 (MB) for oxygen reduction. To optimize the electrocatalytic activity, N-S-CNF-*y* (MB) aerogels were prepared by pyrolyzing BC/MB hybrid aerogels at 600, 700, 800 and 900 °C, respectively. All the N-S-CNF-*y* (MB) aerogels as well as pristine CNF aerogel and commercial Pt/C were investigated by CV. As shown in Fig. 3(b), the N-S-CNF-800 (MB) shows the highest peak current density of 3.16 $\mathrm{mA\cdot cm^{-2}}$, which is significantly higher than those of the other samples, clearly suggesting its superior catalytic activity. These may be ascribed to the combination of a high degree of graphitization and high heteroatom content (Table S2) for N-S-CNF-800 (MB). To gain further insights into the ORR performances of these samples, linear sweep voltammetry (LSV) measurements were performed on a rotating-disk electrode (RDE) (Fig. 3(c)). As expected, N-S-CNF-800 (MB) displays the highest ORR onset potential of –0.210 V among all the carbon-based electrocatalysts, while the onset potentials of CNF-800, N-S-CNF-600 (MB), N-S-CNF-700 (MB), and N-S-CNF-900 (MB) are –0.263 V, –0.256 V, –0.230 V, and –0.242 V, respectively. The ORR reaction current of N-S-CNF-800 (MB) is also higher than those of the other carbon-based electrocatalysts over the whole potential range, agreeing with the CV results. Apart from the positive onset potential and high ORR reaction current, N-S-CNF-800 (MB) possesses the highest diffusion-limited reaction current among all the samples, suggesting a large number of exposed active sites on the material, which can be attributed to a synergistic effect between the 3D interconnected porous network architecture and the large number of N, S heteroatoms in the N-S-CNF-800 (MB) aerogel. However, the electrocatalytic activity of N-S-CNF-800 (MB) aerogel is still inferior to a commercial Pt/C catalyst. To improve its ORR performance, the N-S-CNF-800 (MB) aerogel was further doped by Fe. As showed in Fig. S8 (in the ESM), the as-obtained N-S-CNF-800 (MB)-Fe exhibits much higher catalytic activities than the original N-S-CNF-800 (MB), which can be mainly attributed to the formation of highly active Fe–N–C sites [46, 47]. It may be possible to further improve the activity of N-S-CNF-800 (MB) to compete with the Pt/C catalyst by optimization of experimental conditions, which is our ongoing work.

To gain additional insight into the ORR process on N-S-CNF-800 (MB) electrocatalysts, LSVs were also recorded at different rotation speeds from 225 rpm to 2,500 rpm (Fig. 3(d)). Like most of the studies reported previously [5, 15, 19], the onset ORR potential remains almost constant with increasing rotation rate, but the measured current density shows a typical increase with increasing rotation rate as a result of the faster oxygen flux to the electrode surface. The kinetic parameters can be analyzed with the Koutechy–Levich (K–L) equations. The inset in Fig. 3(d) shows the corresponding K–L plots (j^{-1} vs. $\omega^{-1/2}$) of N-S-CNF-800 (MB), and all the plots show fairly good linearity, suggesting first-order reaction kinetics toward dissolved oxygen and similar electron-transfer number for the ORR process at different potentials. The number of electrons transferred (n) is estimated to be 3.70–3.94 at potentials ranging from –0.45 V to –0.60 V, similar to that of the Pt/C catalyst measured under the same conditions ($n \approx 4.00$, see Fig. S9, in the ESM), indicating that the N-S-CNF-800 (MB) electrode mainly favors a highly efficient four-electron oxygen reduction process throughout the potential range studied.

For practical application in fuel cells, the crossover effect should be considered because fuel molecules (e.g. methanol) may pass through the membrane from anode to cathode and poison the cathode catalyst [8, 10]. Chronoamperometric responses to methanol introduced into an O_2-saturated electrolyte were therefore measured for both N-S-CNF-800 (MB) and the commercial Pt/C catalyst. As shown in Fig. 3(e), an instantaneous current drop was observed for the Pt/C catalyst in O_2-saturated 0.1 M KOH solution after 3 M methanol was added. However, the corresponding amperometric response for the N-S-CNF-800 (MB) electrode remained almost unchanged even after the addition of methanol. Obviously, N-S-CNF-800 (MB) exhibits a high selectivity for ORR with a remarkably good tolerance of crossover effects, thus being superior to the commercial Pt/C catalyst. Furthermore, the durability of the N-S-CNF-800 (MB) and Pt/C catalyst were also evaluated by the chronoamperometric approach, since it is also a major concern in fuel cell technology (Fig. 3(f)). It is observed that the 20,000 s test only caused a slight activity loss (6%) of the

N-S-CNF-800 (MB) catalyst, whereas Pt/C loses up to 31% of its initial activity. These results suggest that the N-S-CNF-800 (MB) aerogel has a much better stability than the Pt/C catalyst. Overall, the absence of a methanol crossover effect and the excellent stability for N-S-CNF-800 (MB) make it a promising potential inexpensive cathodic electrocatalyst for fuel cells.

In addition to the applications for ORR, HDC nanomaterials have been widely used in energy storage devices (e.g. supercapacitors), because doping with heteroatoms results in an improvement in capacitance [11, 20, 22]. To evaluate the properties of our N-S-CNF-*y* (MB) as supercapacitor electrodes, we first carried out CV measurements using a symmetrical two-electrode system in 1 M H_2SO_4 aqueous electrolytes. Figure 4(a) compares the CV curves of CNF-700 and N-S-CNF-*y* (MB) aqueous electrolyte capacitors at a scan rate of 50 $mV \cdot s^{-1}$. Except for N-S-CNF-600 (MB), all samples exhibit roughly rectangular curves which are nearly mirror images, indicating the supercapacitors possess ideal capacitive behavior and good reversibility. The distorted CV behavior of N-S-CNF-600 (MB) can be mainly attributed to its poor graphitization degree. Moreover, compared with other samples, the N-S-CNF-700, 800 (MB) electrodes show higher current densities, representing their high capacitances. Figure 4(b) shows the CV curves of N-S-CNF-700 (MB) aqueous electrolyte capacitors at different scan rates. With the increase of scan rate, the current response increases accordingly and the shapes of the CV curves are retained, indicating a good rate capability. Such excellent capacitive performance of N-S-CNF-700 (MB) electrodes is probably due to the combination of the 3D interconnected network architecture with N, S co-doping.

To reveal the electrochemical capacitive performances of these electrode materials, galvanostatic charge–discharge measurements were carried out at various current densities in a symmetrical two-electrode system with the voltage windows the same as that for the above CV analysis. As shown in Fig. 4(c), the almost symmetric charge–discharge curve of N-S-CNF-700 (MB) reveals a capacitive behavior of EDLC and pseudocapacitance. Meanwhile, the discharging

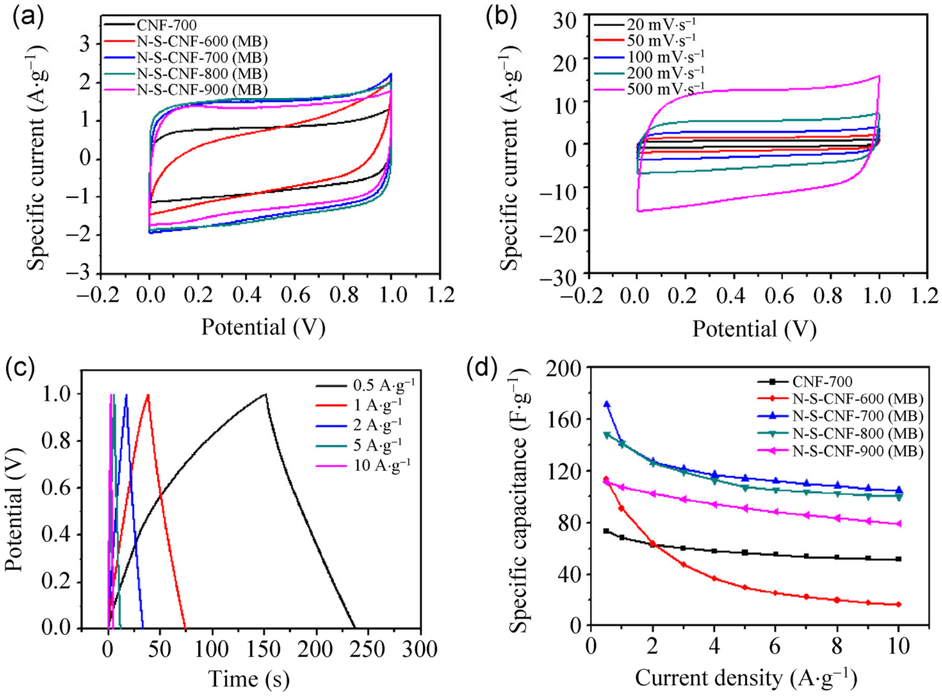

Figure 4 Electrochemical capacitive behaviors of N-S-CNF-*y* (MB) aerogels and CNF-700 aerogel. (a) CV curves of CNF-700, N-S-CNF-600, 700, 800, 900 (MB) in 1 M aqueous H_2SO_4 electrolyte at a scan of 50 $mV \cdot s^{-1}$. (b) CV curves of N-S-CNF-700 (MB) at different scan rates. (c) Galvanostatic charge/discharge curves of N-S-CNF-700 (MB) with different current densities. (d) The variation of specific capacitances of the above samples as a function of current density.

time of the N-S-CNF-700 (MB) is significantly longer compared with those of other materials at both high and low current densities, indicating that the N-S-CNF-700 (MB) offer much larger capacitances (Fig. 4(c) and Fig. S10 in the ESM), which agrees well with those obtained from CV tests (Fig. 4(b) and Fig. S11 in the ESM). The specific capacitances (C_s) of different electrodes calculated based on the galvanostatic discharge data is presented in Fig. 4(d). N-S-CNF-700 (MB) has the highest specific capacitance among all samples at the same current density. For instance, N-S-CNF-700 (MB) possess a specific capacitance of 171.2 $F \cdot g^{-1}$ at 0.5 $A \cdot g^{-1}$, more than twice that of CNF-700 (73.2 $F \cdot g^{-1}$ at 0.5 $A \cdot g^{-1}$) and much higher than the values for N-S-CNF-600, 800, 900 (MB), highlighting the beneficial effects of doping N and S into CNF aerogels and the appropriate choice of carbonization temperature. Notably, the specific capacitance of N-S-CNF-700 (MB) at 10 $A \cdot g^{-1}$ still retains a high value of 105.2 $F \cdot g^{-1}$, while CNF-700, N-S-CNF-600 and N-S-CNF-900 only show capacities of 51.6, 16.4, and 79.2 $F \cdot g^{-1}$, respectively, at the same current density, highlighting the good rate capability of the N-S-CNF-700 (MB)-based supercapacitor. Meanwhile, the N-S-CNF-700 (MB)-based supercapacitor exhibits a high power density and good cycling stability (Fig. S12 in the ESM). Therefore, this carbon material presents great potential for applications in energy storage.

3 Conclusions

We have developed a green, low-cost, versatile and easily scalable method to fabricate various doped CNF aerogels by employing BC pellicles which have adsorbed different toxic organic dyes as precursors. The present method represents a new and fascinating idea, i.e. turning harmful waste into valuable materials, to preparing functional carbon nanomaterials, the first time this has been reported. Moreover, the as-prepared doped CNF aerogels exhibit great potential as electrocatalysts for ORR and as electrode materials for supercapacitors. We believe that the present synthetic idea and strategy can be further extended to develop many other kinds of heteroatom doped or metal/heteroatom co-doped carbon materials in a super environmentally friendly way for various applications, such as photocatalysis, oxygen sensors, and lithium–air batteries.

4 Experimental

4.1 Materials

The raw materials, purified BC pellicles with fiber content of ~1% (vol/vol), were kindly provided by Ms. C. Y. Zhong (Hainan Yeguo Foods Co., Ltd., Hainan, China). All other chemicals were analytical grade and commercially available from Shanghai Chemical Reagent Co. Ltd. and used as received without further purification.

4.2 Preparation of doped CNF aerogels and undoped CNF aerogels (i.e., CNF aerogels)

The white BC pellicles were rinsed several times by deionized water (DIW) before use. Then, the pellicles were cut into rectangular shapes with a sharp blade. The small BC hydrogels were subsequently soaked in different organic dyes solutions (methylene blue, Congo red, acid fuchsin, methyl orange, crystal violet, and Rhodamine B) with a concentration of 1.0 $g \cdot L^{-1}$ for three days, making them adsorb dyes until saturation. Then, the as-obtained BC/dye hybrid hydrogels were frozen in liquid nitrogen (–196 °C) and freeze-dried in a bulk tray dryer (Labconco Corporation, Kansas City, MO, USA) at a sublimating temperature of –50 °C and a pressure of 0.04 mbar. After sublimation of ice, variously colored of BC/dye hybrid aerogels were obtained. Then, the dried BC/ dye hybrid aerogels were transferred into a tubular furnace for pyrolysis under a flowing N_2 atmosphere. The hybrid aerogels precursors were heated to 500 °C at a heating rate of 2 $°C \cdot min^{-1}$, kept this temperature for 1 h, then heated to 600–900 °C at 5 $°C \cdot min^{-1}$ and held at these temperatures for 2 h to allow complete pyrolysis. They were then cooled to 500 °C at 5 $°C \cdot min^{-1}$ and finally cooled to room temperature naturally to yield black doped CNF aerogels. For the purpose of comparison, the CNF aerogels were also prepared. The preparation processes of CNF aerogels were similar to those of the doped CNF aerogels, with the only difference being that the BC pellicles used for preparing CNF aerogel had not adsorbed any dyes.

4.3 Synthesis of N-S-CNF-800 (MB)-Fe

The as-prepared N-S-CNF-800 (MB) aerogels were immersed in 1 mM $FeCl_3$ water/ethanol (vol/vol = 1:4) solution to adsorb Fe^{3+} ions for 24 h. Then they were placed in ambient conditions to dry out. Finally, the hybrid aerogels were subject to annealing at 800 °C in a tubular furnace for 1 h. The as-obtained products are denoted N-S-CNF-800 (MB)-Fe aerogels.

4.4 Characterization

EM images were taken with a Zeiss Supra 40 scanning electron microscope at an accelerating voltage of 5 kV. TEM images were obtained using a Hitachi H7650 transmission electron microscope with a CCD imaging system and an accelerating voltage of 120 kV. High-resolution TEM (HRTEM) and EFTEM mapping were performed using a JEM-ARM 200F microscope operating at an accelerating voltage of 200 kV. Elemental mappings were collected using a Gatan GIF Quantum 965 instrument. XPS were collected on an X-ray photoelectron spectrometer (ESCALab MKII) with an excitation source of Mg Kα radiation (1,253.6 eV). Raman scattering spectra were recorded with a Renishaw System 2000 spectrometer using the 514.5 nm line of an Ar^+ laser for excitation.

4.5 Electrocatalytic measurements

2 mg of the samples were dispersed in a solution containing 0.98 mL of ethanol and 0.02 mL of 5 wt.% Nafion solution, and then ultrasonicated to form a uniform black ink. A certain volume of catalyst ink was then pipetted onto a glassy carbon electrode surface to result in the desired catalyst loading. The catalyst loadings were 0.2 and 0.1 $mg \cdot cm^{-2}$ for carbon-based catalysts and a commercial Pt/C catalyst (20 wt.%, Johnson Matthey), respectively. The electrochemical measurements were carried out in a conventional three-electrode cell using an IM6e electrochemical workstation (Zahner-Electrik, Germany) controlled at room temperature. A glassy carbon (GC) disk with a diameter of 5 mm served as the substrate for the working electrode, with the rotation rate varying from 225 rpm to 2,500 rpm. Ag/AgCl and platinum wire were used as reference and counter electrodes, respectively. All potentials in this study refer to that of the Ag/AgCl (3.5 M KCl) electrode. Before the tests, an O_2 or N_2 flow was passed through the electrolyte in the cell for 30 min to saturate it with O_2 or N_2. The cyclic voltammetry (CV) experiments were performed in N_2- and O_2-saturated 0.1 M aqueous KOH electrolyte solutions with a scan rate of 50 $mV \cdot s^{-1}$. RDE tests were measured in O_2-saturated 0.1 M KOH at 1,600 rpm with a sweep rate of 10 $mV \cdot s^{-1}$.

Electron transfer numbers were calculated using the Koutecky–Levich equation:

$$\frac{1}{j} = \frac{1}{j_L} + \frac{1}{j_K} = \frac{1}{B\omega^{1/2}} + \frac{1}{j_K} \tag{1}$$

$$B = 0.62nFC_0(D_0)^{2/3}\nu^{-1/6} \tag{2}$$

$$j_K = nFkC_0 \tag{3}$$

where j is the measured current density, and j_K and j_L are the kinetic- and diffusion-limiting current densities, respectively. n represents the overall number of electrons gained per O_2, F is the Faraday constant ($F = 96485$ $C \cdot mol^{-1}$), D_0 is the diffusion coefficient of O_2 in 0.1 M KOH electrolyte (1.9×10^{-5} $cm^2 \cdot s^{-1}$), C_0 is the bulk concentration of O_2 (1.2×10^{-6} $mol \cdot cm^{-3}$), ν is the kinetic viscosity of the electrolyte (0.01 $cm^2 \cdot s^{-1}$), ω is the angular velocity of the disk ($\omega = 2\pi N$, N is the linear rotation speed) and k is the electron transfer rate constant.

4.6 Capacitance measurements

A two-electrode configuration consists of two slices of electrode material with the same weights, a cellulose acetate membrane (pore size of 225 nm) as a separator and two Pt foils as the current collectors. Then, the cell assemblies were wrapped with Parafilm. Before the construction of assemblies, the electrodes were soaked in 1 M H_2SO_4 aqueous electrolyte for 12 h. All of the capacitive performances were performed on a CHI 760D electrochemical workstation in 1 M H_2SO_4 solution. The CVs were performed in a voltage window between 0 and 1 V at different scan rates in the range from 20 to 500 $mV \cdot s^{-1}$. The galvanostatic charge–discharge (CD) measurements were carried out in a voltage window the same as that for the above CV analysis under different current density from 0.5 to 10 A·g^{-1}. All electrochemical experiments were carried out at room temperature.

Acknowledgements

This work is supported by the Ministry of Science and Technology of China (Grants 2010CB934700, 2013CB933900, 2014CB931800), the National Natural Science Foundation of China (Grants 21431006, 91022032, 91227103, 21061160492, J1030412), the Chinese Academy of Sciences (Grant KJZD-EW-M01-1), and Hainan Province Science and Technology Department (CXY20130046) for financial support. We thank Ms. C. Y. Zhong for kindly providing purified bacterial cellulose pellicles.

Electronic Supplementary Material: Supplementary material (details of characterization results and electrochemical measurements) is available in the online version of this article at http://dx.doi.org/10.1007/s12274-014-0546-4.

References

[1] Aricò, A. S.; Bruce, P.; Scrosati, B.; Tarascon, J.-M.; van Schalkwijk, W. Nanostructured materials for advanced energy conversion and storage devices. *Nat. Mater.* **2005**, *4*, 366–377.

[2] Orilall, M. C.; Wiesner, U. Block copolymer based composition and morphology control in nanostructured hybrid materials for energy conversion and storage: Solar cells, batteries, and fuel cells. *Chem. Soc. Rev.* **2011**, *40*, 520–535.

[3] Guo, Y.-G.; Hu, J.-S.; Wan, L.-J. Nanostructured materials for electrochemical energy conversion and storage devices. *Adv. Mater.* **2008**, *20*, 2878–2887.

[4] Dai, L. M. Functionalization of graphene for efficient energy conversion and storage. *Acc. Chem. Res.* **2013**, *46*, 31–42.

[5] Liang, Y. Y.; Li, Y. G.; Wang, H. L.; Zhou, J. G.; Wang, J.; Regier, T.; Dai, H. Co_3O_4 nanocrystals on graphene as a synergistic catalyst for oxygen reduction reaction. *Nat. Mater.* **2011**, *10*, 780–786.

[6] Yang, S. B.; Bachman, R. E.; Feng, X. L.; Müllen, K. Use of organic precursors and graphenes in the controlled synthesis of carbon-containing nanomaterials for energy storage and conversion. *Acc. Chem. Res.* **2013**, *46*, 116–128.

[7] Gao, M.-R.; Xu, Y.-F.; Jiang, J.; Yu, S.-H. Nanostructured metal chalcogenides: Synthesis, modification, and applications in energy conversion and storage devices. *Chem. Soc. Rev.* **2013**, *42*, 2986–3017.

[8] Gong, K. P.; Du, F.; Xia, Z. H.; Durstock, M.; Dai, L. M. Nitrogen-doped carbon nanotube arrays with high electrocatalytic activity for oxygen reduction. *Science* **2009**, *323*, 760–764.

[9] Xue, Y. H.; Liu, J.; Chen, H.; Wang, R. G.; Li, D. Q.; Qu, J.; Dai, L. M. Nitrogen-doped graphene foams as metal-free counter electrodes in high-performance dye-sensitized solar cells. *Angew. Chem. Int. Ed.* **2012**, *51*, 12124–12127.

[10] Zhang, C. Z.; Mahmood, N.; Yin, H.; Liu, F.; Hou, Y. L. Synthesis of phosphorus-doped graphene and its multifunctional applications for oxygen reduction reaction and lithium ion batteries. *Adv. Mater.* **2013**, *25*, 4932–4937.

[11] Zhao, L.; Fan, L.-Z.; Zhou, M.-Q.; Guan, H.; Qiao, S. Y.; Antonietti, M.; Titirici, M.-M. Nitrogen-containing hydrothermal carbons with superior performance in supercapacitors. *Adv. Mater.* **2010**, *22*, 5202–5206.

[12] Paraknowitsch, J. P.; Thomas, A. Doping carbons beyond nitrogen: An overview of advanced heteroatom doped carbons with boron, sulphur and phosphorus for energy applications. *Energy Environ. Sci.* **2013**, *6*, 2839–2855.

[13] Zheng, Y.; Jiao, Y.; Ge, L.; Jaroniec, M.; Qiao, S. Z. Two-step boron and nitrogen doping in graphene for enhanced synergistic catalysis. *Angew. Chem. Int. Ed.* **2013**, *52*, 3110–3116.

[14] Silva, R.; Voiry, D.; Chhowalla, M.; Asefa, T. Efficient metal-free electrocatalysts for oxygen reduction: Polyaniline-derived N- and O-doped mesoporous carbons. *J. Am. Chem. Soc.* **2013**, *135*, 7823–7826.

[15] Yang, D.-S.; Bhattacharjya, D.; Inamdar, S.; Park, J.; Yu, J.-S. Phosphorus-doped ordered mesoporous carbons with different lengths as efficient metal-free electrocatalysts for oxygen reduction reaction in alkaline media. *J. Am. Chem. Soc.* **2012**, *134*, 16127–16130.

[16] Chen, P.; Xiao, T.-Y.; Qian, Y.-H.; Li, S.-S.; Yu, S.-H. A nitrogen-doped graphene/carbon nanotube nanocomposite with synergistically enhanced electrochemical activity. *Adv. Mater.* **2013**, *25*, 3192–3196.

[17] Zheng, Y.; Jiao, Y.; Jaroniec, M.; Jin, Y. G.; Qiao, S. Z. Nanostructured metal-free electrochemical catalysts for highly efficient oxygen reduction. *Small* **2012**, *8*, 3550–3566.

[18] Liu, R. L.; Wu, D. Q.; Feng, X. L.; Müllen, K. Nitrogen-doped ordered mesoporous graphitic arrays with high electrocatalytic activity for oxygen reduction. *Angew. Chem. Int. Ed.* **2010**, *49*, 2565–2569.

[19] Liang, J.; Jiao, Y.; Jaroniec, M.; Qiao, S. Z. Sulfur and nitrogen dual-doped mesoporous graphene electrocatalyst for oxygen reduction with synergistically enhanced performance. *Angew. Chem. Int. Ed.* **2012**, *51*, 11496–11500.

[20] Chen, L.-F.; Zhang, X.-D.; Liang, H.-W.; Kong, M. G.; Guan, Q.-F.; Chen, P.; Wu, Z.-Y.; Yu, S.-H. Synthesis of nitrogen-doped porous carbon nanofibers as an efficient electrode material for supercapacitors. *ACS Nano* **2012**, *6*, 7092–7102.

[21] Zhu, H.; Yin, J.; Wang, X. L.; Wang, H. Y.; Yang, X. R. Microorganism-derived heteroatom-doped carbon materials for oxygen reduction and supercapacitors. *Adv. Funct. Mater.* **2013**, *23*, 1305–1312.

[22] Wu, Z.-S.; Winter, A.; Chen, L.; Sun, Y.; Turchanin, A.; Feng, X. L.; Müllen, K. Three-dimensional nitrogen and boron Co-doped graphene for high-performance all-solid-state supercapacitors. *Adv. Mater.* **2012**, *24*, 5130–5135.

[23] Wang, H. B.; Maiyalagan, T.; Wang, X. Review on recent progress in nitrogen-doped graphene: Synthesis, characterization, and its potential applications. *ACS Catal.* **2012**, *2*, 781–794.

[24] Tang, Y. F.; Allen, B. L.; Kauffman, D. R.; Star, A. Electrocatalytic activity of nitrogen-doped carbon nanotube cups. *J. Am. Chem. Soc.* **2009**, *131*, 13200–13201.

[25] Qu, L. T.; Liu, Y.; Baek, J.-B.; Dai, L. M. Nitrogen-doped graphene as efficient metal-free electrocatalyst for oxygen reduction in fuel cells. *ACS Nano* **2010**, *4*, 1321–1326.

[26] Zhang, C. H.; Fu, L.; Liu, N.; Liu, M. H.; Wang, Y. Y.; Liu, Z. F. Synthesis of nitrogen-doped graphene using embedded carbon and nitrogen sources. *Adv. Mater.* **2011**, *23*, 1020–1024.

[27] Deng, D. H.; Pan, X. L.; Yu, L.; Cui, Y.; Jiang, Y. P.; Qi, J.; Li, W.-X.; Fu, Q.; Ma, X. C.; Xue, Q. K.; Sun, G. Q.; Bao, X. H. Toward N-doped graphene via solvothermal synthesis. *Chem. Mater.* **2011**, *23*, 1188–1193.

[28] Panchakarla, L. S.; Subrahmanyam, K. S.; Saha, S. K.; Govindaraj, A.; Krishnamurthy, H. R.; Waghmare, U. V.; Rao, C. N. R. Synthesis, structure, and properties of boron- and nitrogen-doped graphene. *Adv. Mater.* **2009**, *21*, 4726–4730.

[29] Geng, D. S.; Chen, Y.; Chen, Y. G.; Li, Y. L.; Li, R. Y.; Sun, X. L.; Ye, S. Y.; Knights, S. High oxygen-reduction activity and durability of nitrogen-doped graphene. *Energy Environ. Sci.* **2011**, *4*, 760–764.

[30] Wang, X. R.; Li, X. L.; Zhang, L.; Yoon, Y.; Weber, P. K.; Wang, H. L.; Guo, J.; Dai, H. J. N-doping of graphene throughelectrothermal reactions with ammonia. *Science* **2009**, *324*, 768–771.

[31] Sheng, Z.-H.; Shao, L.; Chen, J.-J.; Bao, W.-J.; Wang, F.-B.; Xia, X.-H. Catalyst-free synthesis of nitrogen-doped graphene via thermal annealing graphite oxide with melamine and its excellent electrocatalysis. *ACS Nano* **2011**, *5*, 4350–4358.

[32] Yu, D. S.; Zhang, Q.; Dai, L. M. Highly efficient metal-free growth of nitrogen-doped single-walled carbon nanotubes on plasma-etched substrates for oxygen reduction. *J. Am. Chem. Soc.* **2010**, *132*, 15127–15129.

[33] Gupta, V. K.; Kumar, R.; Nayak, A.; Saleh, T. A.; Barakat, M. A. Adsorptive removal of dyes from aqueous solution onto carbon nanotubes: A review. *Adv. Colloid Interfac.* **2013**, *193–194*, 24–34.

[34] Gupta, V. K.; Suhas. Application of low-cost adsorbents for dye removal–A review. *J. Environ. Manage.* **2009**, *90*, 2313–2342.

[35] Crini, G. Non-conventional low-cost adsorbents for dye removal: A review. *Bioresource Technol.* **2006**, *97*, 1061–1085.

[36] Mezohegyi, G.; van der Zee, F. P.; Font, J.; Fortuny, A.; Fabregat, A. Towards advanced aqueous dye removal processes: A short review on the versatile role of activated carbon. *J. Environ. Manage.* **2012**, *102*, 148–164.

[37] Iguchi, M.; Yamanaka, S.; Budhiono, A. Bacterial cellulose—A masterpiece of nature's arts. *J. Mater. Sci.* **2000**, *35*, 261–270.

[38] Yano, H.; Sugiyama, J.; Nakagaito, A. N.; Nogi, M.; Matsuura, T.; Hikita, M.; Handa, K. Optically transparent composites reinforced with networks of bacterial nanofibers. *Adv. Mater.* **2005**, *17*, 153–155.

[39] Wu, Z.-Y.; Li, C.; Liang, H.-W.; Chen, J.-F.; Yu, S.-H. Ultralight, flexible, and fire-resistant carbon nanofiber aerogels from bacterial cellulose. *Angew. Chem. Int. Ed.* **2013**, *52*, 2925–2929.

[40] Liang, H.-W.; Guan, Q.-F.; Zhu, Z.; Song, L.-T.; Yao, H.-B.; Lei, X.; Yu, S.-H. Highly conductive and stretchable conductors fabricated from bacterial cellulose. *NPG Asia Mater.* **2012**, *4*, e19.

[41] Chen, L.-F.; Huang, Z.-H.; Liang, H.-W.; Guan, Q.-F.; Yu, S.-H. Bacterial-cellulose-derived carbon nanofiber@MnO_2 and nitrogen-doped carbon nanofiber electrode materials: An asymmetric supercapacitor with high energy and power Density. *Adv. Mater.* **2013**, *25*, 4746–4752.

[42] Wu, G.; Nelson, M.; Ma, S. G.; Meng, H.; Cui, G. F.; Shen, P. K. Synthesis of nitrogen-doped onion-like carbon and its use in carbon-based CoFe binary non-precious-metal catalysts for oxygen-reduction. *Carbon* **2011**, *49*, 3972–3982.

[43] Yang, S. B.; Feng, X. L.; Wang, X. C.; Müllen, K. Graphene-based carbon nitride nanosheets as efficient

metal-free electrocatalysts for oxygen reduction reactions. *Angew. Chem. Int. Ed.* **2011**, *50*, 5339–5343.

[44] Su, Y. Z.; Zhang, Y.; Zhuang, X. D.; Li, S.; Wu, D. Q.; Zhang, F.; Feng, X. L. Low-temperature synthesis of nitrogen/sulfur co-doped three-dimensional graphene frameworks as efficient metal-free electrocatalyst for oxygen reduction reaction. *Carbon* **2013**, *62*, 296–301.

[45] Yang, S. B.; Zhi, L. J.; Tang, K.; Feng, X. L.; Maier, J.; Müllen, K. Efficient synthesis of heteroatom (N or S)-doped graphene based on ultrathin graphene oxide-porous silica sheets for oxygen reduction reactions. *Adv. Funct. Mater.* **2012**, *22*, 3634–3640.

[46] Lefèvre, M.; Proietti, E.; Jaouen, F.; Dodelet, J.-P. Iron-based catalysts with improved oxygen reduction activity in polymer electrolyte fuel cells. *Science* **2009**, *324*, 71–74.

[47] Wu, G.; More, K. L.; Johnston, C. M.; Zelenay, P. High-performance electrocatalysts for oxygen reduction derived from polyaniline, iron, and cobalt. *Science* **2011**, *332*, 443–447.